2020

ESTIMATION OF ATMOSPHERIC CONDITIONS OVER A LONG HORIZONTAL PATH USING MULTI-FRAME BLIND DECONVOLUTION (MFBD) TECHNIQUES IN COMPARISON WITH DELAYED TILT ANISOPLANATISM (DELTA) SOFTWARE

Hannah Stoll

ESTIMATION OF ATMOSPHERIC CONDITIONS OVER A LONG HORIZONTAL PATH USING MULTI-FRAME BLIND DECONVOLUTION (MFBD) TECHNIQUES IN COMPARISON WITH DELAYED TILT ANISOPLANATISM (DELTA) SOFTWARE

By

Hannah M. Stoll

A THESIS

Submitted in partial fulfillment of the requirements for the degree of

MASTER OF SCIENCE

In Electrical Engineering

MICHIGAN TECHNOLOGICAL UNIVERSITY

2020

This thesis has been approved in partial fulfillment of the requirements for the Degree of MASTER OF SCIENCE in Electrical Engineering.

Department of Electrical and Computer Engineering

Thesis Advisor:	*Dr. Michael C. Roggemann*
Committee Member:	*Dr. Timothy J. Schulz*
Committee Member:	*Dr. Glen E. Archer*
Department Chair:	*Dr. Glen E. Archer*

Dedication

To my family, coaches, teachers, and friends

who encouraged and pushed me to be the person I am today.

Contents

List of Figures

List of Tables

Acknowledgments

I would like to give a special thanks to my advisor, Dr. Mike Roggemann, for giving me the opportunity to learn and expand my skill set. Thank you to my committee members and all of my professors along the way, my friends, family, teammates, and my coaches who have taught me so many life lessons. Lastly, thank you to all of those who believed in me, and those who didn't, you were my motivators and kept me focused in my studies when I needed it the most.

List of Abbreviations

CCD	Charge-Coupled Device
CMOS	Complementary Metal-Oxide Semiconductor
DELTA	Delayed Tilt Anisoplanatism
GPF	Generalized Pupil Function
HEL	High Energy Lasers
IFOV	Instantaneous Field of View
L-BFGS	Limited-Memory Boyden-Fletcher-Goldfarb-Shanno
MFBD	Multi-Frame Blind Deconvolution
MSE	Mean-Squared Error
OTF	Optical Transfer Function
PSF	Point Spread Function

Abstract

The potential to track and view objects in space from the ground with greater near real time knowledge of the intervening turbulence would be a revolutionary capability. The objective of this thesis is to cross-validate two separate methods used to estimate the Fried parameter. This verification is a step toward a commercial grade product that would make real-time estimates of the turbulence strength along an optical path from a ground-based observatory to a satellite in orbit around the Earth. Michigan Technological University has developed a multi-frame blind deconvolution (MFBD) algorithm used to estimate r_0 and it was tested against MZA's Delayed Tilt Anisoplanatism (DELTA) software. Important realizations about MFBD initialization parameters were made during this study. Key results from the study included that approximately 62% of the final MTU r_0 estimates were in between the DELTA r_0A and r_0B estimates. Only 8.3% of all of the results are more than 1 cm outside of the r_0A and r_0B range. The outcome of these experiments has shown that overall the MTU results fall very close to or within the range of the estimated DELTA results.

Chapter 1

Introduction

1.1 Scope

The goal for this thesis is to experimentally verify a method that will ultimately progress to the level of a commercial grade product in order to make real-time estimates of the turbulence strength along an optical path from a ground-based observatory to a satellite in orbit around the Earth. This ability would benefit a vast amount of fields, but using it for military operations and astronomy are the main focus here. It would aid the military branches in defense and surveillance, where as it would be a great new resource for scientists or civilians interested in astronomy. The potential to track and view objects in space from the ground with greater near real

time knowledge of the intervening turbulence would be a revolutionary capability.

Light propagating through the atmosphere is strongly affected by turbulent motion of air. The physical mechanism which gives rise to this effect is a combination of differential heating of the Earth, the buoyancy of air, and the low kinematic viscosity of air causing randomly sized and shaped pockets of air with uniform temperature, referred to as turbulent eddies, to be constantly mixing. Since the index of refraction of air is very sensitive to temperature, and as a result the index of refraction of the atmosphere is constantly and randomly changing in space and time. Optical systems experience this as a time varying aberration which strongly limits the ability to focus light which has passed through the atmosphere, or project laser beams through the atmosphere without using advanced adaptive optics systems. Adaptive optical system performance can be optimized based on knowledge of the turbulence statistics [1]. The goal of this thesis research project was to conduct an outdoor experimental data gathering and processing campaign to experimentally validate a technique that had been previously demonstrated only in simulation.

The previously developed technique is based on multi-frame blind deconvolution (MFBD). In MFBD multiple short exposure images of the target are measured and then processed in a non-linear optimization-based algorithm to jointly estimate both the object and the aberrations associated with each image. In the past the goal was to obtain the best possible image, and the aberration parameter estimates were

nuisance parameters that had to be computed as part of the MFBD processing. However, in the simulation work leading to this project it was shown that the aberration parameters could be used to estimate the turbulence strength [2].

Our corporate partner for the project, MZA Corp. of Dayton, OH, has independently developed a similar capability and packaged it in a camera and processing system they call DELTA. For operational reasons not relevant to this thesis it was desirable to compare performance of DELTA with the MFBD-based technique. With this in mind we developed a measurement and processing system that would allow us to make this comparison with real data gathered over the 3 km horizontal path between the Dow building on the Michigan Technological University campus and the Huntington Bank building in Hancock, MI.

The key results of this thesis are that MTU's estimates more closely follow r_0A than r_0B. About two thirds of the MTU results were in between r_0A and r_0B. The average of the majority of the estimates was around 3 cm.

The remainder of this thesis is organized as follows:

1. Verification: a brief description of MZA and MTU's software.

2. Background: an in-depth explanation of the mathematics and theory behind MFBD and the Fried Parameter.

3. Methods: the procedures taken to set up data collection and the reasoning behind parameter assumptions.

4. Results: graphical comparisons of MTU and MZA's r_0 estimations.

5. Conclusion and Future Work: discussion surrounding overall results and opportunities to expand on based off of this thesis.

1.2 Verification

MZA Associates Corporation is collaborating with Michigan Technological University to accomplish this goal. MZA is known for working with High Energy Lasers (HEL) and advanced optical systems. MTU has vast experience in research with image processing techniques. Combining past projects and experience allows for the cross-verification of two methods that determine interesting characteristics of the atmosphere.

1.2.1 MZA's DELTA Software

MZA is the developer of the DELTA Imaging Path Turbulence Monitor, which has been verified and commercialized for up to two kilometers in path distance [3]. It needs to be modified to be accurate at longer distances, so testing it and cross-validating

the results with a separate method MTU has will expand that path potential. This system views a stationary object with several trackable features, and then it estimates the non-uniform $C_n^2(z)$ profile associated with the atmospheric turbulence between the sensors and the target [4]. This refractive-index structure parameter profile is derived using path-weighting functions along the known propagation path. The atmospheric coherence width, better known as Fried's parameter, is another useful descriptor of atmospheric turbulence information. The focus of this study revolves around the estimation of Fried's parameter, r_0, which can be used in the calculation of $C_n^2(z)$ [5].

1.2.2 MTU's MFBD Code

MTU has developed a post-processing code that inputs a stack of distorted images and uses a multi-frame blind deconvolution technique to reconstruct an average image while estimating r_0 over a mean squared error curve. This method will be explained in detail in later sections. The minimum MSE is the best resulting conclusion for the Fried parameter over the set of images processed. With this in mind, the MTU MFBD and MZA DELTA results for r_0 can be compared over a few hours span of time [2].

A rigorous comparison between MZA's DELTA method and MTU's MFBD technique to estimate the Fried parameter will cross-validate the systems and allow for an

accurate representation of atmospheric conditions across a long horizontal path.

Chapter 2

Background Information

2.1 Multi-Frame Blind Deconvolution

Multi-frame blind deconvolution is a process that jointly estimates an image along with the image's point spread function. There are many assumptions that must be made in order to use this technique. These will be explained later on, as a better understanding of the method as a whole is needed first.

MFBD takes a stack of images as its input. These images are corrupted by both atmospheric turbulence and Gaussian noise that is produced within all CCD/CMOS imaging systems. The standard linear imaging model shown below in equation 2.1 is the basis that this entire process stems from.

$$d_k(\vec{x}) = o(\vec{x}) * s_k(\vec{x}) + n_k(\vec{x}) \tag{2.1}$$

The object, $o(\vec{x})$, is constant and unchanging. The vector $s_k(\vec{x})$ represents the optical system's individual point spread functions for each image. The convolution of the two eludes to a set of images that are corrupted by turbulence, but have no measurement noise. The noise must be accounted for, so it is added to the estimate as $n_k(\vec{x})$ which is zero mean Gaussian noise with the same standard deviation at every pixel. The term $d_k(x)$ defines the k'th image in the stack [6]. The PSF's have a special relationship with the generalized pupil function where the modulus squared of the Fourier transform of the GPF is equal to the PSF. This association, shown in equation 2.2 is relevant, since the PSF's in this case are unknown and need to be estimated for MFBD.

$$s_k(\vec{x}) = |\mathcal{F}[H_k(\vec{u})]|^2 \tag{2.2}$$

The vector $\vec{x}$ is a coordinate in the image plane calculated by:

$$\vec{f} = \frac{\vec{x}}{\lambda f_l} \tag{2.3}$$

Lambda is the mean wavelength and f_l is the focal length of the imaging system. Now, the generalized pupil function is key because it is used to describe turbulence effects on imaging systems. The GPF is shown below.

$$H_k(\vec{u}) = |H(\vec{u})|e^{j\phi_k(\vec{u})} \tag{2.4}$$

The vector $\vec{u}$ is a 2-D coordinate in pupil space where as $\phi_k(\vec{u})$ is a parameter representing the different phase aberrations in the imaging system. These phase aberrations can be expressed in terms of summing Zernike orthonormal functions together. Using Zernike polynomials in this sense accounts for the many fixed and random aberrations that occur in imaging systems due to diffraction and path length variability. The summing function is expressed below in equation 2.5.

$$\tilde{\phi}_k(\vec{u}, \vec{\alpha}_k) \approx \sum_{j=1}^{J} \alpha_{j,k}\phi_j(\vec{u}) \tag{2.5}$$

The Zernike basis functions $\phi_j(\vec{u})$ are weighted by the corresponding coefficients $\alpha_{j,k}$, which are referred to as Zernike coefficients. These Zernike coefficients are random Gaussian numbers with a unity variance and mean of 0.5. These Zernikes can be implemented into the general pupil function to create the relationship shown in equation 2.6.

$$H_k(\vec{u}, \vec{\alpha}_k) = |H(\vec{u})| e^{j\tilde{\phi}_k(\vec{u}, \vec{\alpha}_k)} \tag{2.6}$$

Now, remembering the association seen in equation 2.2, the PSF can be expressed as the inverse Fourier transform of the new GPF. This allows for the estimation of the k'th aberrated PSF as a vector of weighted Zernike polynomials.

$$s_k(\vec{x}, \vec{\alpha}_k) = |\mathcal{F}[H_k(\vec{u}, \vec{\alpha}_k)]|^2 \tag{2.7}$$

Using the Gaussian noise model, each image $d_k(x)$ can be approximated as a random variable that has a Gaussian probability density function.

$$d_k(x) = o(\vec{x}) * s_k(\vec{x}) + n_k(\vec{x}) \tag{2.8}$$

For simplification purposes, let $g_k(\vec{x}, \vec{\alpha}_k)$ be the noise free image that would be present if the object is $o(\vec{x})$ and the aberrations were represented by $\vec{\alpha}_k$:

$$g_k(\vec{x}, \vec{\alpha}_k) = o(\vec{x}) * s_k(\vec{x}, \vec{\alpha}_k) \tag{2.9}$$

The likelihood function of the k^{th} image is thus the Gaussian PDF for the noise. The

probability density function of this Gaussian noise model is shown below in equation 2.10. The estimate of the object is represented as $f(\vec{x}, \vec{\alpha_k})$.

$$p[d_k(\vec{x}); f(\vec{x}, \vec{\alpha}_k)] = \frac{1}{(2\pi\sigma_n^2)^{1/2}} \exp\left\{ - \frac{[d_k(\vec{x}) - g_k(\vec{x}, \vec{\alpha}_k)]^2}{2\pi\sigma_n^2} \right\} \tag{2.10}$$

The likelihood of this PDF for the entire data set is represented in equation 2.11. This encompasses the likelihood of the complete data set consisting of all the pixel intensities in all the corrupted images.

$$p[d_k(\vec{x}); f(\vec{x}, \vec{\alpha}_k)] = \prod_{k=1}^{K} \prod_{x \epsilon \chi} \frac{1}{(2\pi\sigma_n^2)^{1/2}} \exp\left\{ - \frac{[d_k(\vec{x}) - g_k(\vec{x}, \vec{\alpha}_k)]^2}{2\pi\sigma_n^2} \right\} \tag{2.11}$$

To simplify this analysis, the natural log of the likelihood function can be taken in order to change products into summations. This Gaussian log-likelihood seen in equation 2.12 is easier to use for further calculations.

$$L[f(\vec{x}, \vec{\alpha}_k)] = - \sum_{k=1}^{K} \sum_{x \epsilon \chi} [d_k(\vec{x}) - g_k(\vec{x}, \vec{\alpha}_k)]^2 \tag{2.12}$$

The limited-memory Broyden-Fletcher-Goldfarb-Shanno optimization maximizes the log-likelihood function by incorporating the gradient in its analytic form with respect

to pixel intensities.

$$\frac{\partial}{\partial f} L[f(\vec{x}, \vec{\alpha}_k)] = 2 \sum_{k=1}^{K} \sum_{x \epsilon \chi} [d_k(\vec{x}) - g_k(\vec{x}, \vec{\alpha}_k)] \frac{\partial}{\partial f} g_k(\vec{x}, \vec{\alpha}_k)) \tag{2.13}$$

It also must be represented in terms of the Zernike coefficients which gives way to the equation shown below.

$$\frac{\partial}{\partial \vec{\alpha}} L[f(\vec{x}, \vec{\alpha}_k)] = 2 \sum_{k=1}^{K} \sum_{x \epsilon \chi} [d_k(\vec{x}) - g_k(\vec{x}, \vec{\alpha}_k)] \frac{\partial}{\partial \vec{\alpha}} g_k(\vec{x}, \vec{\alpha}_k) \tag{2.14}$$

L-BFGS optimization maximizes this cost function in terms of the true object, the phase terms, and the Zernike coefficients. It requires an estimate of the gradient of the log-likelihood function shown previously. It estimates the Hessian by maintaining the recent estimates of the gradient and the current image intensity. Then using Matlab, nonlinear optimization is conducted to locate the values of the object and aberration coefficients that were most likely to have caused those particular distorted images. It uses the Zernike coefficients as an initial guess to iterate on estimates of the object and PSF before outputting the r_0 with the smallest MSE.

The MSE is calculated by comparing the average OTF obtained from the set of Zernike coeffients estimated in the course of the MFBD run to the theoretical long

exposure OTF which is a function of the Fried parameter r_0. The long exposure OTF is given by:

$$\mathcal{H}(\vec{f}, r_0) = \mathcal{H}_{DL}(\vec{f}) \exp\left\{ -3.44 \left(\frac{\lambda f_l |\vec{f}|}{r_0} \right)^{5/3} \right\} \tag{2.15}$$

where $\mathcal{H}_{DL}(\vec{f})$ is the diffraction limited OTF, and f_l is the focal length of the imaging system. It is important to note that $\mathcal{H}(\vec{f}, r_0)$ can be computed from knowledge of the optical system, and is a strong function of r_0. The average OTF associated with the image data $\tilde{\mathcal{H}}(\vec{f})$ be estimated using equation 2.6 to compute the estimated generalized pupil function for each frame after the MFBD run, then computing the OTF for each frame as described in [7]. It must be noted that the estimated OTF is also a function of r_0, the number of frames used K and the number of iterations N_I. Hence we will write the estimated OTF going forward to make this dependence explicit as $\tilde{\mathcal{H}}(\vec{f}, N_I, K)$ The MSE used to estimate r_0 is given by

$$MSE(r_0, N_I, K) = \sum_{|\vec{f}| \leq 10 \text{ samples}} \left[\left| \tilde{\mathcal{H}}(\vec{f}, N_I, K) - \mathcal{H}(\vec{f}, r_0) \right|^2 \right] \tag{2.16}$$

Limiting the band over which $MSE(r_0, N_I, K)$ is computed was found to be very important in the Phase I program because the high frequency estimates of the OTF are quite noisy under almost every condition of interest. After the MFBD calculation

$MSE(r_0, N_I, K)$ is computed for a range of r_0 values, and the value of r_0 which minimizes the error is chosen as the estimated r_0.

2.2 Atmospheric Turbulence Related Parameters

When attempting to characterize the turbulent atmosphere, this paper will focus on a comparison of Fried's parameter. The effective aperture radius of an imaging system is commonly defined by this parameter, also called the atmospheric coherence radius, r_0. Fried, Roggemann, and Welsh define this mathematically in equation 2.18.

$$r_0 = 0.185\left[\frac{4\pi^2}{k^2 \int_0^L (\frac{L-z}{L})^{5/3} C_n^2(z) dz}\right]^{3/5} \tag{2.17}$$

The wave number, k, is defined as $k = 2\pi/\lambda$, where λ is the mean wavelength across the path. The integral's limits are the distance from the pupil plane to the scene, $z = 0$ and $z = L$. This equation is simplified by assuming that the refractive-index structure constant over the horizontal path. The formula for calculating Fried's parameter in this case is

$$r_0 = (0.16k^2 C_n^2 L)^{3/5} \tag{2.18}$$

Physically, r_0 represents the largest diameter telescope for which diffraction limited resolution would be obtained in the presence of turbulence characterized by r_0 [7].

Chapter 3

Methods for MTU MFBD Processing

3.1 Optical Path, Target, and Data Collection

A long horizontal path of just over three kilometers was chosen to test these atmospheric turbulence conditions through imaging. According to Google Earth this path is 3018 m in length, and it is approximately 25 m above the surface of the Earth. The path is shown below in figure 3.1.

Located on the ninth floor of MTU's Dow building, images were taken with an Celestron VX 11 Schmidt-Cassegrain telescope equipped with a FLIR Grasshopper3 USB3

Figure 3.1: Google Earth Image of the Path From the Huntington Bank Building in Hancock, MI to the Dow Building on the MTU Campus

Mono Vision camera. This system pointed out toward the Huntington Bank building across the Portage canal. Unfortunately, the telescope had to be moved inside due to winter weather, but data through the window still suffices as a valid comparison of the two methods. This indoor viewing area is shown in figure 3.2. A setup with a patterned target was constructed on top of the bank building, and it can be seen in figure 3.3.

The main features of the target are the spokes, which are approximately 36 inches in diameter, and the black patch in the lower left, which has a point-like source in the center. The spoke target, and the surrounding apparatus on the roof of the bank provided ample opportunities for testing out MFBD and DELTA codes to estimate r_0. The goal of the point source was to provide a direct estimate of the average point spread function of the turbulence which would allow for an independent measurement of r_0 to be computed and compared to the MFBD outputs. Many target and light

Figure 3.2: Image of the Indoor Telescope Setup

combinations were attempted, but there was too much leakage from the light source to add this third metric to the validation.

Ultimately, combined with the DELTA software, this test setup was used to collect uncompressed TIFF images that would later be inputs to MTU's MFBD post-processing code. The data was collected by first aligning the telescope onto the target. Then using the camera's USB connection to a laptop, the DELTA software could be connected to the system. Location geometry including latitude, longitude, and altitude of the sensor and target were necessary for the process DELTA uses to estimate it's outputs. Observation parameters and telescope information such as instantaneous

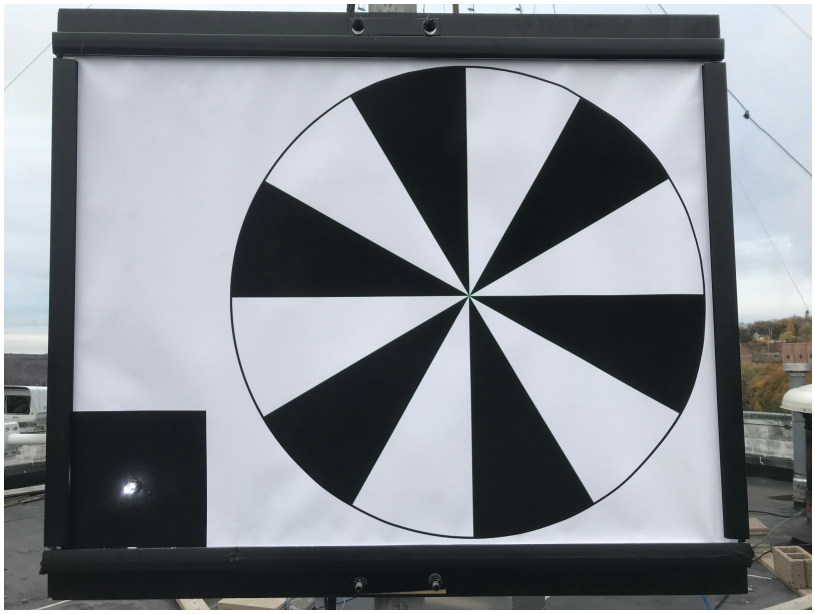

Figure 3.3: Photograph of a Version of the Spoke Target on Top of the Bank Building

field of view (IFOV), wavelength, and diameters had to be inputted into the software. The shutter and gain were automatic to allow for changes in daylight over a span of time. The input parameters are shown in tables 3.1-3.5.

Table 3.1
Platform Location Geometry

	Latitude	*Longitude*	*Altitude*
Degree	47	88	649
Minute	7	32	
Second	12	47	
Direction	North	West	

With these inputs entered, Delta could be run for several hours at a time. For the purposes relevant to this thesis, it was used to capture data for approximately 2 hour intervals. A longer period of time was not used due to the uncompressed images

Table 3.2
Target Location Geometry

	Latitude	*Longitude*	*Altitude*
Degree	47	88	692
Minute	7	35	
Second	34	7	
Direction	North	West	

Table 3.3
Camera Settings

Camera Options		*Image Options*	
Auto Exposure	*Frame Rate (fps)*	*Image Size (pix)*	*Pixel Format*
1.00	100	800x800	Raw

Table 3.4
Observation and Telescope Parameters

IFOV (μrad)	*Lambda* (nm)	*Dobs* (m)	*D* (m)
1.23	550	0.056	0.279

Table 3.5
Data Recording

Recording Interval	*Format*
300 frames every 2 min	Uncompressed TIFF

requiring a lot of storage space. Sets of 300 images are taken every 2 minutes and saved. This length of time is still enough to display results useful in comparison of DELTA's processing with MTU's processing method.

3.2 Post Processing

3.2.1 Assumptions for MFBD

Several steps were taken in order to reduce the processing time from hours to minutes, and to eliminate to the maximum extent possible the effects of wind buffeting for outdoor data, and building instabilities due to air handlers and elevator activity in the indoor setting. The approach to these issues contains the following elements:

1. Choosing a square subframe of the data which contains the target but removes most of the background in the images. We have for now settled on 250×250 pixel subimages. The size of this subimage is user-selected before a run. Since the angular sampling of the measurement system is constant, it is likely that the subimage size will change with target size and range.

2. Choosing a "search window" bigger than the square subimage and implementing a spatial cross correlation-based approach for sensing the line-of-sight jitter and removing it.

3. Modifying the MFBD code to run at the same angular sampling as the measurement system, rather than upsampling to slighty higher than the Nyquist frequency for the data.

4. Finding a reasonable number of iterations and initial Zernike coefficients for the purposes of the estimating r_0 at the minimum MSE.

Now, each of these issues is discussed in further detail.

An 800×800 pixel full image and the 250×250 subimage extracted from one frame of data is shown in figure 3.4. It was necessary to select a number of images to process, which in this case is 50. To remove the effects of line of sight jitter, and likely some of the effects of global atmospheric tilt, a search band of 30 pixels was established around the 250×250 subimage to yield a 310×310 pixel image. The 50 images to be processed were then averaged to create a 310×310 pixel reference image used for sensing shifts.

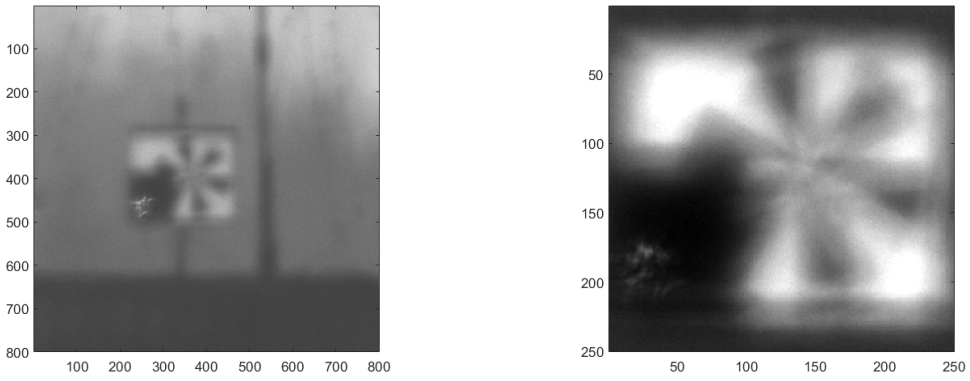

(a) Full Image (b) Aligned Image

Figure 3.4: Example of a Full 800 × 800 Pixel Image and the Associated Cropped 250 × 250 Image Used for Processing

The spatial cross correlation between each image in the data set was to be processed

and compared to the reference image. The location of the peak of the cross correlation is a reasonable measure of the shift between the image being processed and the reference. The image being processed was shifted to place its centroid in the same location as the centroid of the reference image, and then it was cropped to 250×250 pixels. This process was applied to each of the 50 images in the data set to prepare the images for MFBD processing.

We originally had been running the MFBD code with upsampled data as the combination of aperture diameter, f-number, and pixel pitch results in the raw data being slightly undersampled from the perspective of the Nyquist theorem. To get to Nyquist sampling we were upsampling by a factor of two, and then interpolating. There were two problems with this: (1) In some cases it created a 500×500 image which has four times the number of pixels as the original data set and hence increased run times dramatically; and (2) there are artifacts from the interpolation which are unavoidable in the processing paradigm, and would affect MFBD reconstruction at higher frequencies. The decision was made to modify the code to run at the sampling of the data collection system as a means of improving run times. Note that this approach has an effect on the high spatial frequencies in the reconstructed images, but the intuition was that estimating r_0 accurately requires that only the low frequencies be reconstructed well, and this intuition has initially proven to be correct.

Extensive testing was conducted in order to choose the number of Zernike coefficients

and number of iterations that were used in this study. These tests were done using 50 images from the March 17, 2020 data set. The table below shows experiments that tested if the MSE and r0 results were greatly affected by the initial number of Zernike coefficients chosen.

Table 3.6
Results for MSE and r_0 Over A Range of Zernikes at 50 Iterations

Number of Zernikes	*MSE*	r_0 (m)
100	1.3932	0.034
90	1.3171	0.035
60	1.1561	0.039
50	0.95926	0.041
30	1.1629	0.050
20	0.82263	0.057
10	0.44727	0.059
5	1.3808	0.1

The results from table 3.6 were semi-predictable. For 50 iterations, the MSE drastically decreases as the number of Zernikes is lowered. The cutoff is at 10 Zernikes, as the MSE starts to increase again at any lower than this. Finding that the smaller number of Zernike coefficients has a significantly lower MSE makes sense with the results from Dr. Archer's paper, where he uses 30 Zernikes for his work [8]. It is interesting to see that the values for r_0 increased as the number of Zernikes decreased. After acquiring these outputs, the effect that the number of iterations had on the same Zernike scale was desired. Table 3.7 shows the same test at 100 iterations to see how the error would change.

Table 3.7
Results for MSE and r_0 Over A Range of Zernikes at 100 Iterations

Number of Zernikes	*MSE*	r_0 (m)
100	1.1199	0.030
90	1.1181	0.031
60	1.0422	0.036
50	1.0838	0.037
30	1.2344	0.044
20	0.91001	0.052
10	0.57644	0.056
5	0.75777	0.1

This test surprisingly resulted in more error from 50 Zernikes down to 10 Zernikes at the higher number of iterations. At the smaller number of iterations the error was smaller at the higher number of Zernikes. Overall, the lowest MSE was consistently at 10 Zernikes for both cases of iterations. From these results, it would be assumed that 10 Zernikes would cause the least MSE and therefore would be used for all comparison processing. Another remaining question was how a full range of the number of iterations changed at a constant value of 10 Zernikes. Table 3.8 represents this test.

Based off of the outcome of this test, the general trend is that the MSE is seen to increase as the number of iterations increases. This holds true from 20-100 iterations. At 10 iterations the MSE increases again. The overall minimum MSE is at 20 iterations.

Now that these parameters could be assumed, it was desired to have an error metric

Table 3.8
Results for MSE and r_0 Over A Range of Iteration Numbers at A Constant Value of 10 Zernikes

Number of Iterations	*MSE*	r_0 (m)
10	0.49532	0.1
20	0.097411	0.1
30	0.24324	0.075
40	0.34254	0.067
50	0.46735	0.058
60	0.5189	0.058
70	0.48037	0.058
80	0.49802	0.057
90	0.55197	0.056
100	0.62227	0.052

associated with each r_0 estimate at these settings. A final test was conducted to examine how much the MSE and r_0 outputs changed when run several times at the same parameter settings. Table 3.9 shows the experiment to obtain these error bars.

Table 3.9
Error metric results from testing the same parameters to see how much variability occurred

Number of Zernikes	*Number of Iterations*	*MSE*	r_0 (m)
10	20	0.097411	0.1
10	20	0.10043	0.097
10	20	0.10342	0.099
10	20	0.10069	0.098
10	20	0.10098	0.098
10	20	0.097411	0.01
10	20	0.10043	0.097
10	20	0.10342	0.099
10	20	0.10069	0.098
10	20	0.10098	0.098
Error = (max-min)		0.006009	0.003

Based on this analysis, it was assumed that using 10 Zernikes and 20 iterations per r_0 estimate would be the most accurate option for processing. The MSE can vary $\pm$ 0.006009, causing the estimate of r_0 to have an error metric of $\pm$ 0.003 meters associated with it. A total of 50 frames per 300 image directory was used in processing each r_0 estimate over time. DELTA processes these 300 image data sets right after they are collected each time and saves that information in a results file which is turned into a summary file after all collection is finished. This way those r_0 results could be plotted on top of MTU's results in MATLAB.

There was, however, reason to be concerned about using only 10 Zernikes for these calculations. The main issue is the estimated r_0 values that resulted from this choice were quite a lot higher than the DELTA estimates, and seemed inconsistent the the visual quality of the images from previous simulations. We conjecture that this a consequence of 10 Zernikes simply not being able to capture the high spatial frequency content of the incident turbulence-corrupted wave. Hence, we eventually decided to put a floor on the number of Zernikes at 50, and explore how this worked. Both of these approaches are reported in the next Chapter.

Chapter 4

Results and Discussion

4.1 First comparison of Fried Parameter Results Between MTU and DELTA's Processing Methods

MTU's processing code was run on several days worth of data sets and the results were graphed as point plots. Estimates of r_0 were plotted every 10 minutes over approximately a 2 hour time span each day. They were plotted against DELTA's r_{0A} and r_{0B} outputs. Examples of unprocessed images from the first and last timestamp are displayed to help gauge what kind of conditions occurred over the entire time

span. Results are displayed and discussed below in figure's 4.1-4.10.

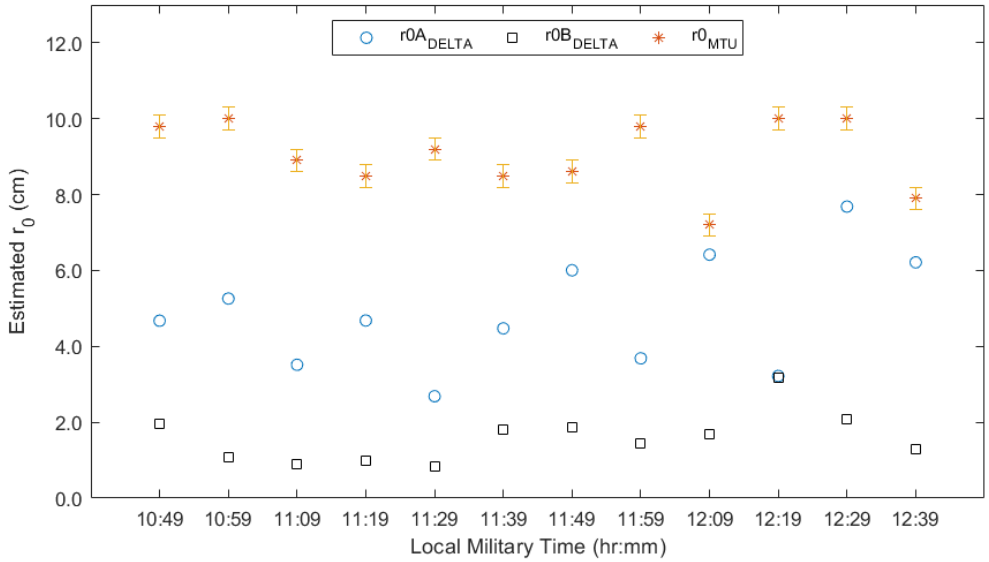

Figure 4.1: Comparison of Estimated r_0 over Time for 03-17-2020

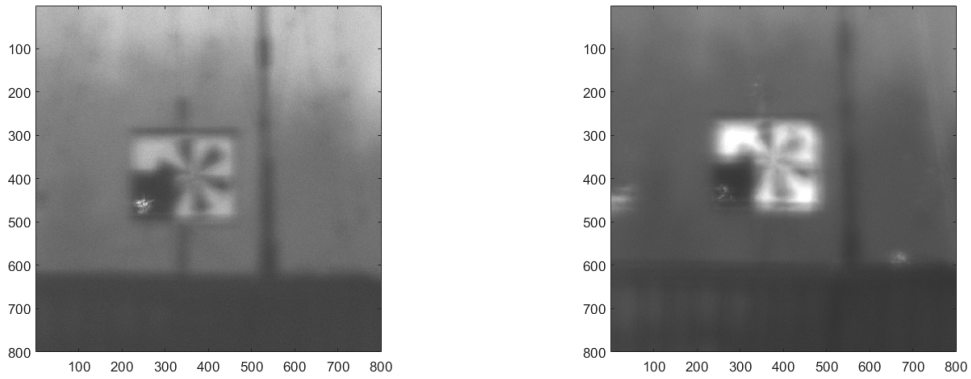

(a) Image from First Timestamp Set

(b) Image from Last Timestamp Set

Figure 4.2: First Images from the First Timestamp and Last Timestamp Processed on 03-17-2020

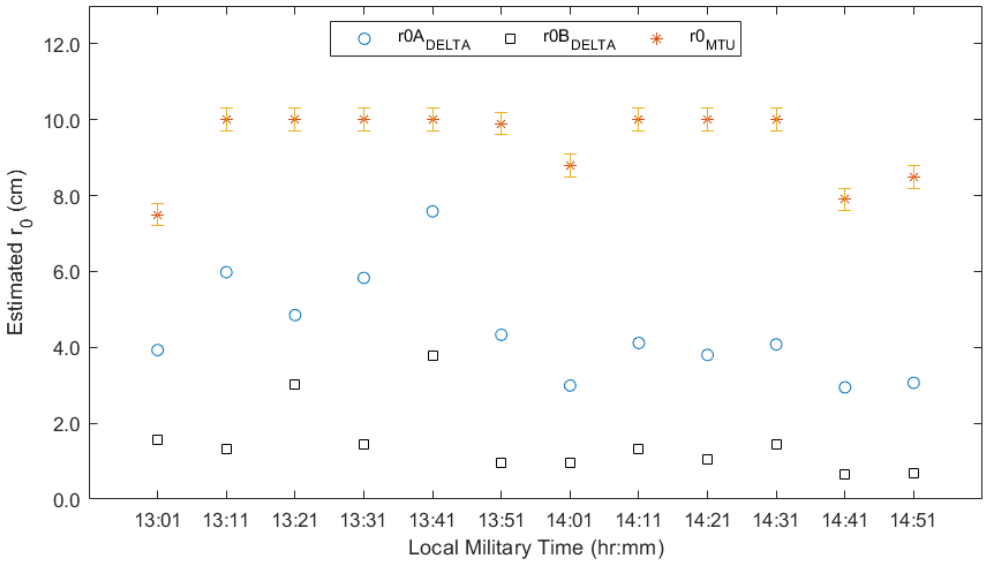

Figure 4.3: Comparison of Estimated r_0 over Time for 03-18-2020

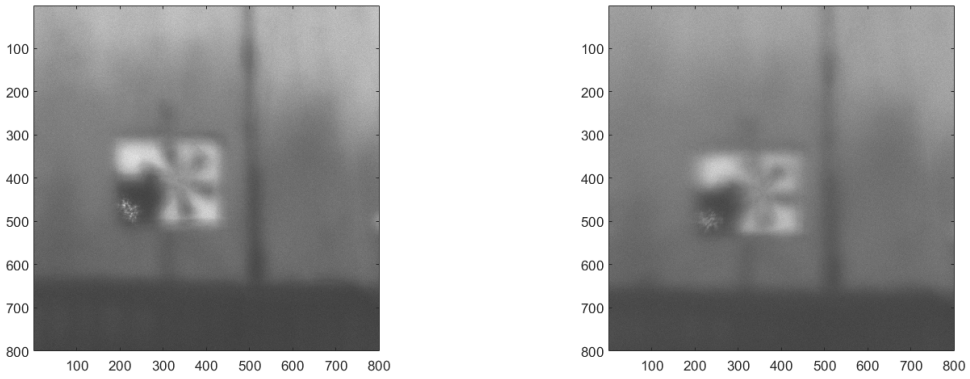

(a) Image from First Timestamp Set

(b) Image from Last Timestamp Set

Figure 4.4: First Images from the First Timestamp and Last Timestamp Processed on 03-18-2020

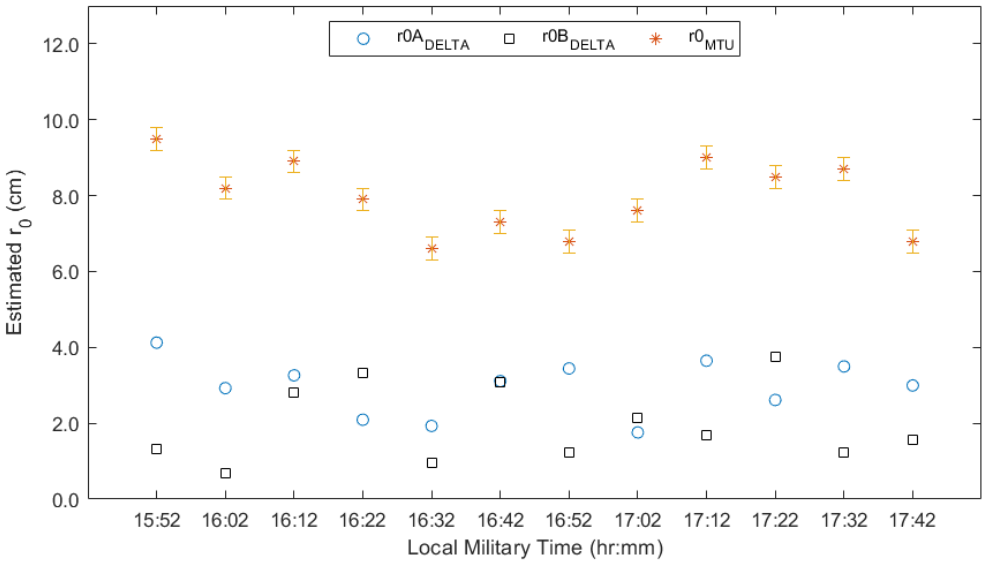

Figure 4.5: Comparison of Estimated r_0 over Time for 03-20-2020

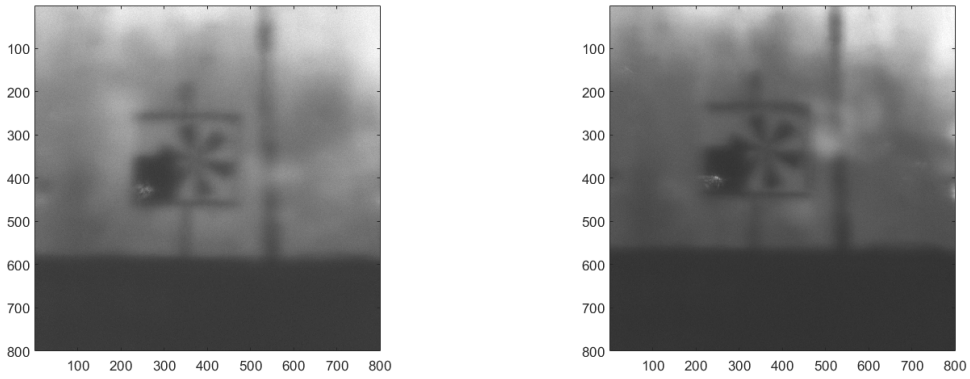

(a) Image from First Timestamp Set

(b) Image from Last Timestamp Set

Figure 4.6: First Images from the First Timestamp and Last Timestamp Processed on 03-20-2020

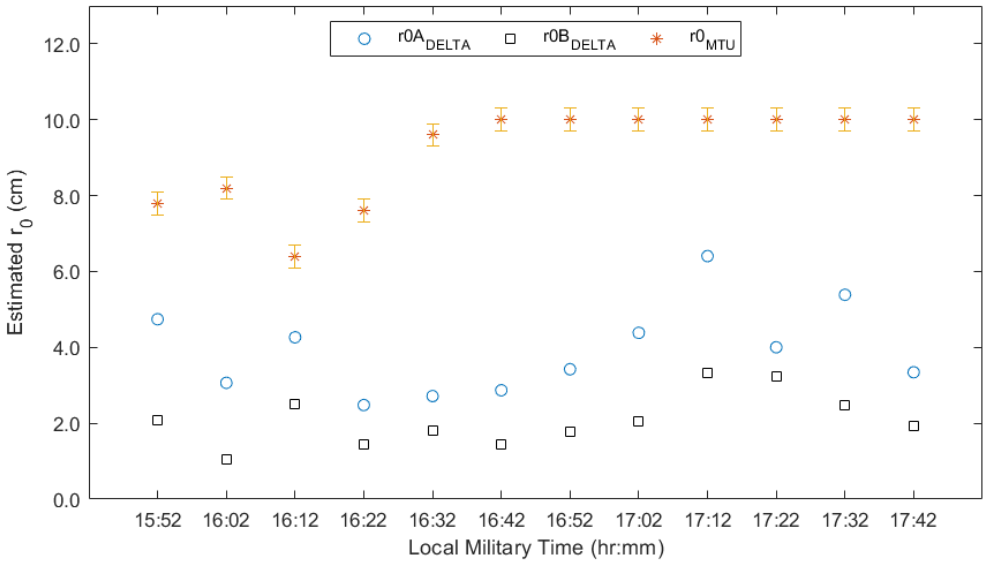

Figure 4.7: Comparison of Estimated r_0 over Time for 03-21-2020

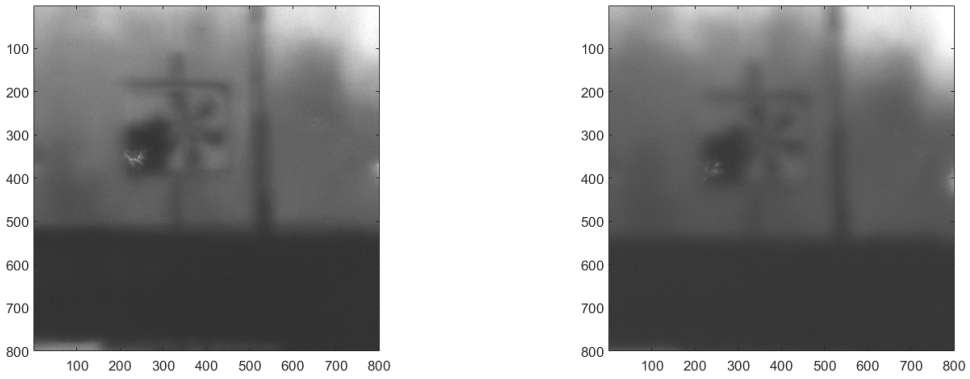

(a) Image from First Timestamp Set

(b) Image from Last Timestamp Set

Figure 4.8: First Images from the First Timestamp and Last Timestamp Processed on 03-21-2020

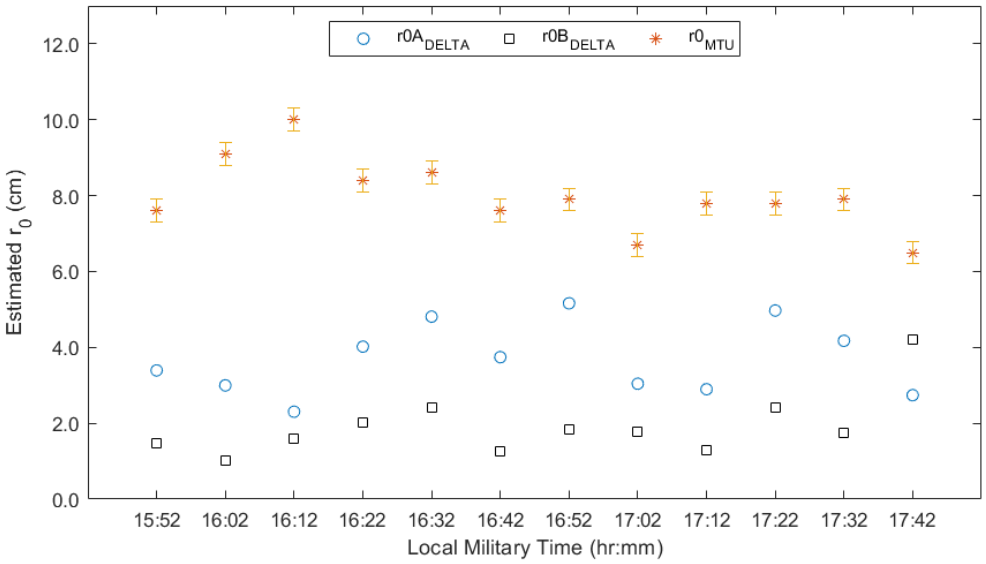

Figure 4.9: Comparison of Estimated r_0 over Time for 03-22-2020

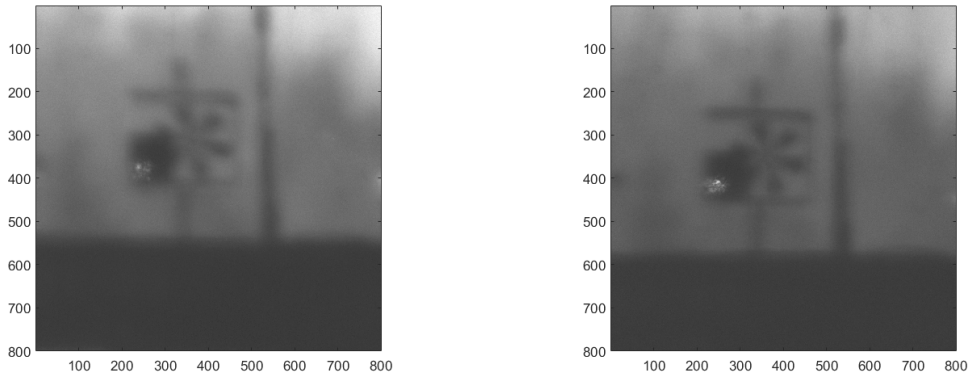

(a) Image from First Timestamp Set

(b) Image from Last Timestamp Set

Figure 4.10: First Images from the First Timestamp and Last Timestamp Processed on 03-22-2020

Judging from these results, it may have been overlooked that even though the MSE appeared smaller, using 10 Zernikes was most likely inaccurate. So, more tests were run assuming that not using enough Zernikes smooths over the data and doesn't account for all of the turbulence. In order to gauge a more accurate representation of the data, an experiment was conducted using 50 and 60 Zernikes respectively to see how the number of iterations was affected. This number of Zernikes is enough to account for the majority of the turbulence in the data without smoothing everything over too much. Tables 4.1 and 4.2 show these tests.

Table 4.1
Results for MSE and r_0 Over A Range of Iteration Numbers at A Constant Value of 50 Zernikes

Number of Iterations	*MSE*	r_0 (m)
10	0.50343	0.067
20	0.72523	0.056
30	1.0649	0.045
40	1.1839	0.044
50	1.1663	0.042
60	1.115	0.041
70	1.1362	0.039
80	1.0345	0.039
90	1.0993	0.038
100	1.0203	0.037

A few test runs were completed at 90 Zernikes as well, but from these results and the previous tests shown in the methods section the r_0 estimates didn't change drastically from what they were with less Zernikes and higher iterations. Based on these results, as the number of Zernike coefficients increases, the r_0 estimates tend to decrease.

Table 4.2
Results for MSE and r_0 Over A Range of Iteration Numbers at A Constant Value of 60 Zernikes

Number of Iterations	*MSE*	r_0 (m)
10	0.6543	0.062
20	0.91948	0.051
30	1.1841	0.043
40	1.1352	0.041
50	1.1117	0.038
60	1.127	0.038
70	1.1462	0.037
80	1.0924	0.036
90	1.114	0.036
100	1.0904	0.035

Further tests would need to be conducted to display the range this effect has. For the purposes of this thesis, both tables 4.1 and 4.2 showed a decrease in MSE at 60 iterations. In general, a higher number of iterations means more accurate results. Due to time constraints on processing and the fact that the MSE didn't change much at these levels of Zernikes, iterations 30-100 were all decent parameter choices. The MSE at 10 and 20 iterations was very low, and the r_0 estimates jumped up more drastically, so this most likely meant there weren't enough iterations to grasp a very accurate estimation. Since there was a small decrease in MSE at 60 iterations that parameter would be used for the next round of tests. The code ran faster at 50 Zernikes and the MSE was still technically smaller at that setting than at 60, so that would be used as well to compare to DELTA.

4.2 Final Comparison of Fried Parameter Results Between MTU and DELTA's Processing Methods

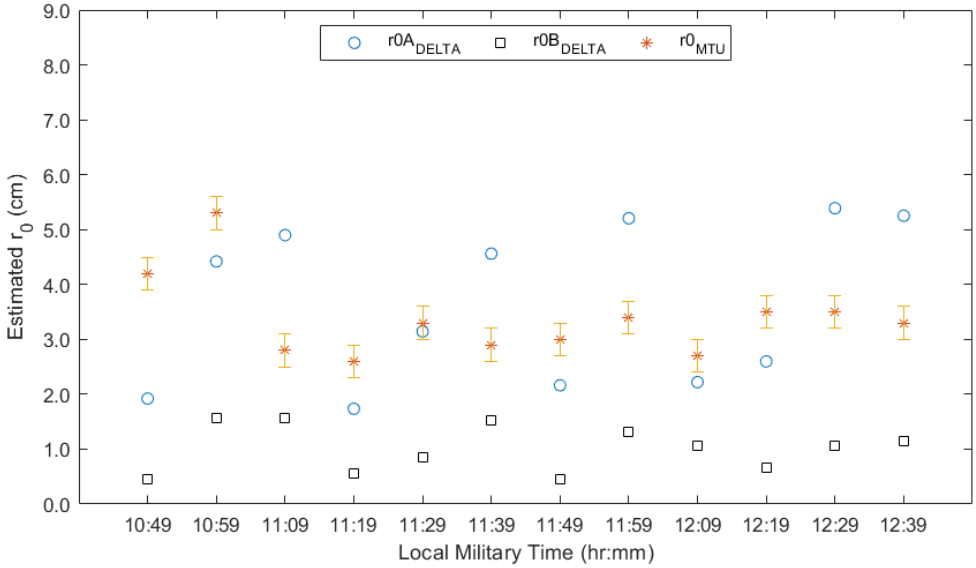

Figure 4.11: Final Comparison of Estimated r_0 over Time for 03-17-2020

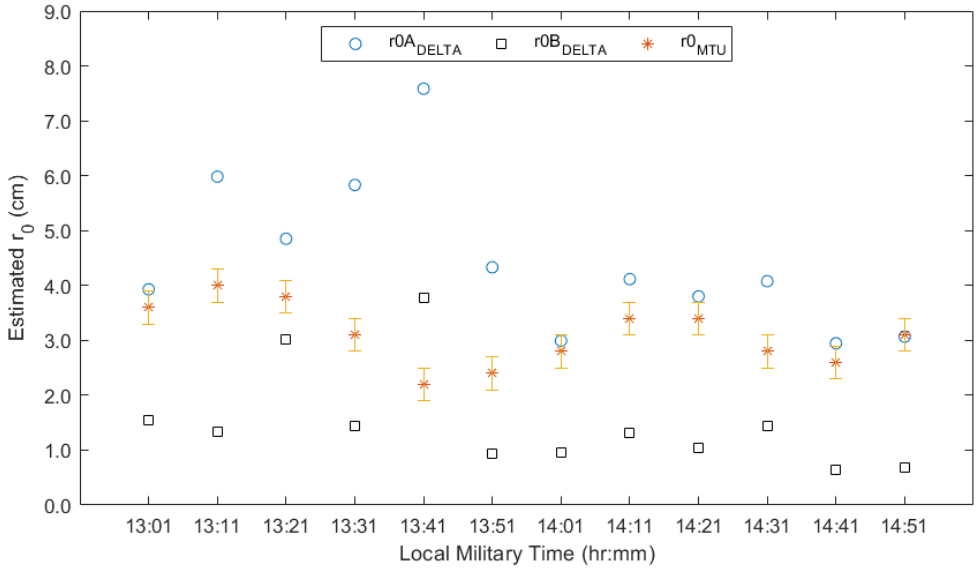

Figure 4.12: Final Comparison of Estimated r_0 over Time for 03-18-2020

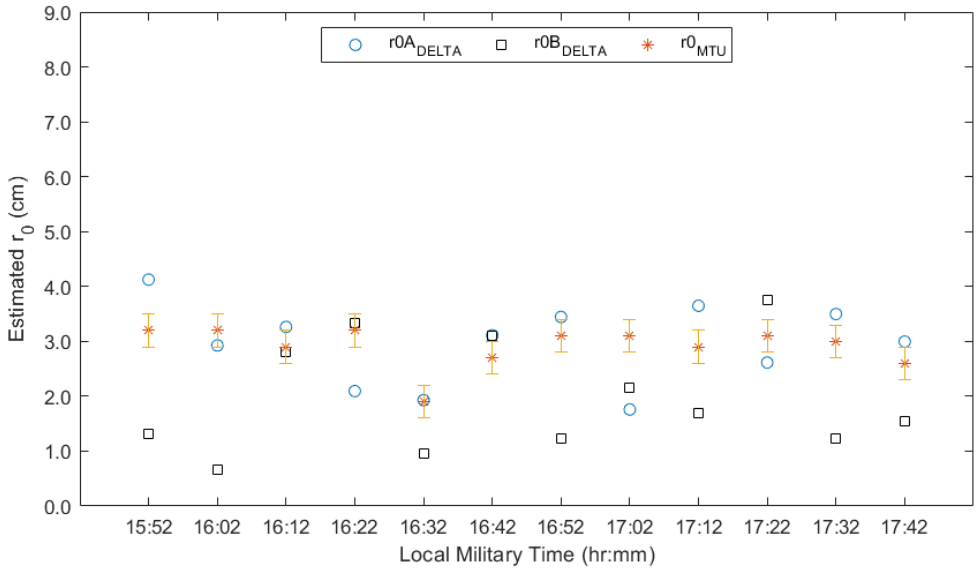

Figure 4.13: Final Comparison of Estimated r_0 over Time for 03-20-2020

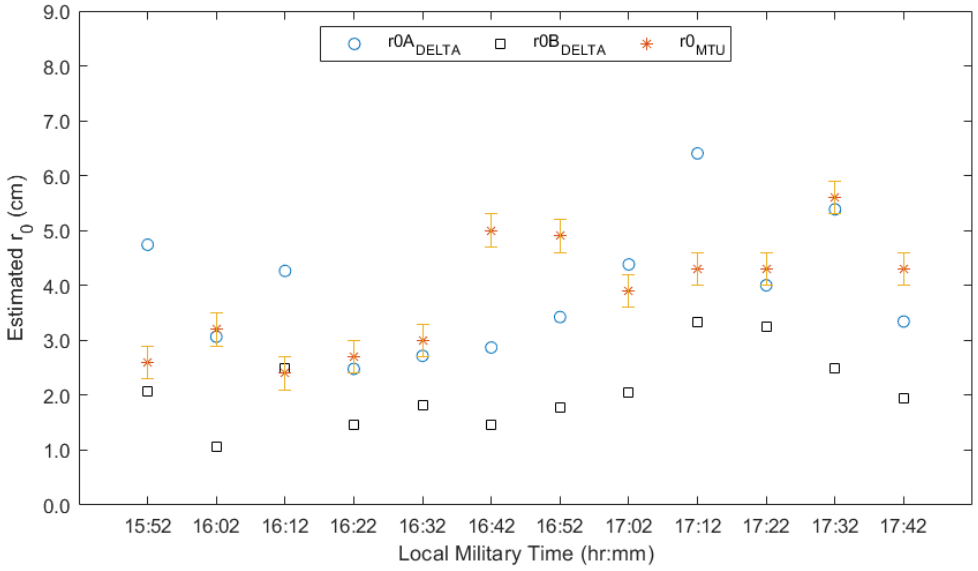

Figure 4.14: Final Comparison of Estimated r_0 over Time for 03-21-2020

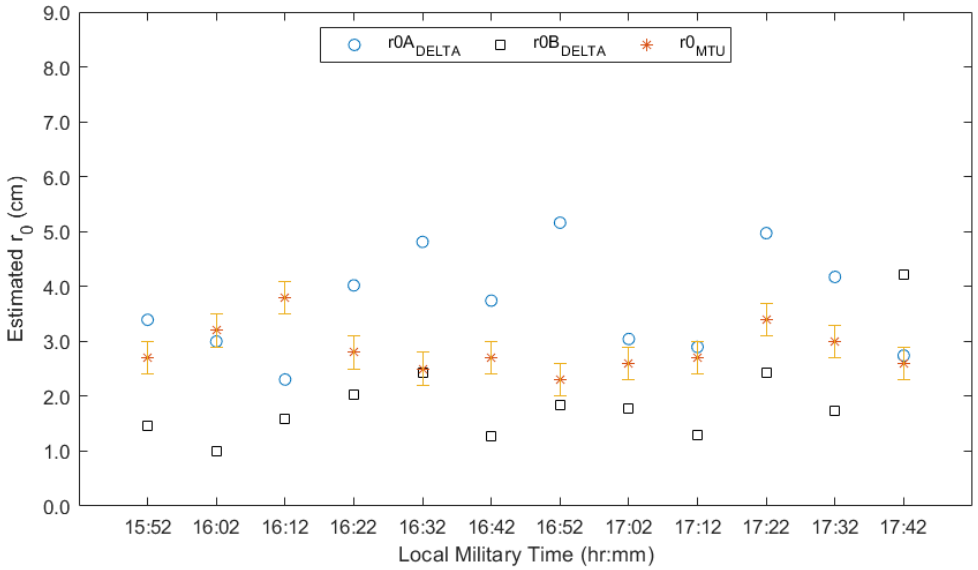

Figure 4.15: Final Comparison of Estimated r_0 over Time for 03-22-2020

Now, these results are much more accurate and appear to be closer to the DELTA estimates. Approximately 62% of the final MTU r_0 estimates were in between the DELTA r_0A and r_0B estimates. Comparing the two, around 72% of the final MTU r_0 estimates were closer to r_0A than they were to r_0B. Of all of MTU's estimates, 58% of them were within 1 cm of r_0A. Only 8.3% of all of the results are more than 1 cm outside of the r_0A and r_0B range. The outcome of these experiments has shown that overall the MTU results fall very close to or within the range of the estimated DELTA results.

Chapter 5

Conclusion and Future Work

Judging from the results plots comparing MTU and DELTA's estimates of the Fried parameter, there are many conclusions to be made. These realizations are described below, and have given way to the possibility of future experiments on this area of study.

5.1 Conclusion

Ultimately, the first attempt at comparisons were concluded to be inaccurate due to a smoothing effect that failed to encompass all of the atmospheric turbulence at an extremely low number of Zernikes. Ten Zernike coefficients was just not enough to

account for all of the turbulence. Expanded testing with consideration of minimums in MSE gave way to a new choice of start up parameters for a secondary round of comparisons.

The final refined MTU results using 50 Zernike coefficients and 60 iterations matched up with DELTA's r_0A estimates quite well. Over half of MTU's results were in between the range of r_0A and r_0B. DELTA's r_0A appeared to be more closely related to MTU's estimates than the r_0B estimate was. Less than one tenth of the results were outside of the DELTA range by over one centimeter, giving good reason to believe that the vast majority of the estimates were accurate. In conclusion, cross-validation has shown that the MTU results fall very close to or within the range of the estimated DELTA results.

This experiment proved that there can be a large change in result accuracy due to a few seemingly arbitrary initialization parameters in MFBD. For the purposes of this thesis, comparing MTU's results to MZA's DELTA estimations showed just how much variability there is and brought up these interesting realizations. Overall, more work that includes a true r_0 validation method should be conducted to get a firm grasp on what start up parameters provide results with the least amount of error.

5.2 Future Work

This work opened up a lot of questions about how the number of Zernikes and iterations affects MSE and r_0 estimates in MTU's MFBD code. A great way to come to a conclusion on these vague parameters would be to have a true r_0 calculation to tweak the code results to. One example of how this could be achieved would be to use a point source method with a very large black target around it as was talked about in the background section of this thesis. This way, the PSF's would be calculated instead of estimated and "truth" would be known. To add to this, more testing on a range of iterations for specific Zernike values is also desired. This would allow for a possible end cap on the lowest that the r_0 estimate would go before hitting a floor. There was just not enough time to get all of these questions answered in this specific thesis. This future work would open up great opportunities to validate important initialization parameters and provide extreme confidence in MTU's MFBD post processing code.

References

[1] M. C. Roggemann and B. M. Welsh, *Imaging Through Turbulence*. CRC Press, 1996.

[2] G. Archer, "Application of mfbd algorithms to image reconstruction under anisoplanatic conditions," 01 2013.

[3] J. E. McCrae, S. R. Bose-Pillai, and S. T. Fiorino, "Estimation of turbulence from time-lapse imagery," *Optical Engineering*, vol. 56, no. 7, pp. 1 – 9, 2017.

[4] M. R. Whiteley, D. C. Washburn, and L. A. Wright, "Differential-tilt technique for saturation-resistant profiling of atmospheric turbulence," in *Adaptive Optics Systems and Technology II* (R. K. Tyson, D. Bonaccini, and M. C. Roggemann, eds.), vol. 4494, pp. 221 – 232, International Society for Optics and Photonics, SPIE, 2002.

[5] L. C. Andrews and R. L. Phillips, *Laser Beam Propagation Through Random Media*. Bellingham: SPIE Optical Engineering Press, 2 ed., 2005.

[6] C. L. Matson, K. Borelli, S. Jefferies, J. Charles C. Beckner, E. K. Hege, and M. Lloyd-Hart, "Fast and optimal multiframe blind deconvolution algorithm for high-resolution ground-based imaging of space objects," *Appl. Opt.*, vol. 48, pp. A75–A92, Jan 2009.

[7] G. Archer, J. Bos, and M. C. Roggemann, "Comparison of bispectrum, multiframe blind deconvolution and hybrid bispectrum-multiframe blind deconvolution image reconstruction techniques for anisoplanatic, long horizontal-path imaging," *Optical Engineering*, vol. 53, p. 043109, 04 2014.

[8] G. Archer, J. Bos, and M. C. Roggemann, "Reconstruction of long horizontal-path images under anisoplanatic conditions using multiframe blind deconvolution," *Optical Engineering*, vol. 52, pp. 083108–083108, 08 2013.

[9] M. C. Roggemann and T. J. Schulz, "Algorithm to increase the largest aberration that can be reconstructed from hartmann sensor measurements," *Applied optics*, vol. 37, pp. 4321–9, 08 1998.

[10] M. C. Roggemann, T. J. Schulz, C. Wai Ngai, and J. T. Kraft, "Joint processing of hartmann sensor and conventional image measurements to estimate large aberrations: Theory and experimental results," *Applied optics*, vol. 38, pp. 2249–55, 05 1999.

Appendix A

Added Results From A Slightly Different Target Format

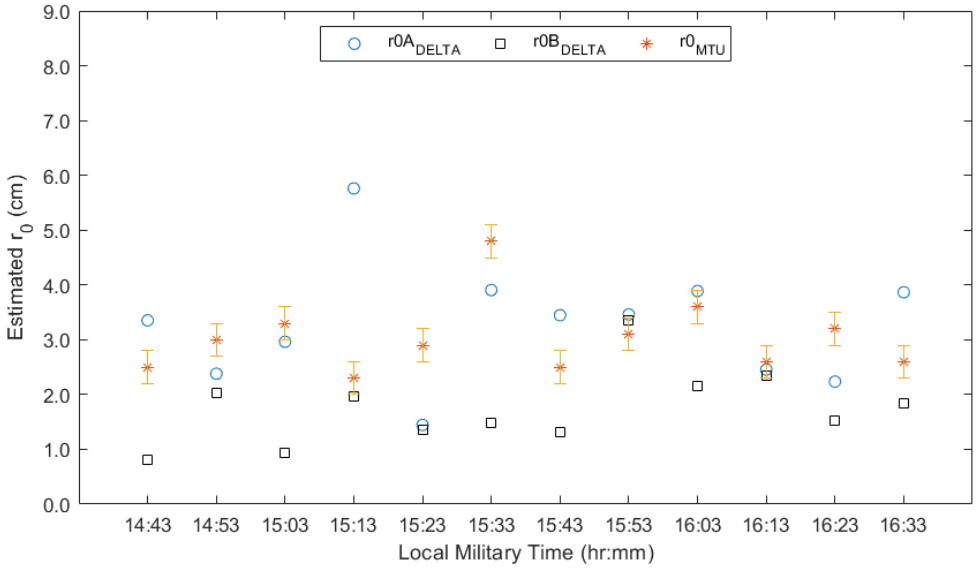

Figure A.1: Comparison of Estimated r_0 over Time for 02-24-2020

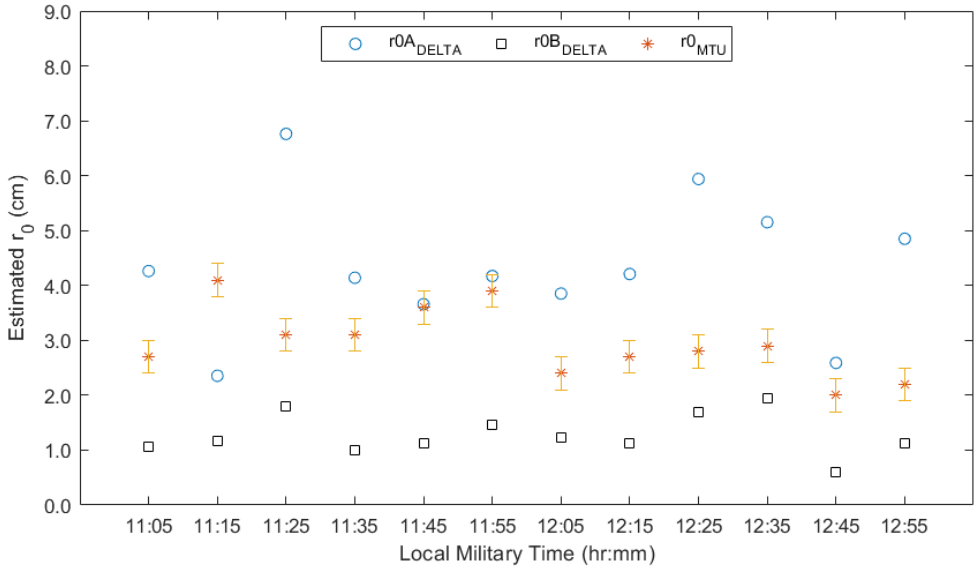

Figure A.2: Comparison of Estimated r_0 over Time for 02-25-2020

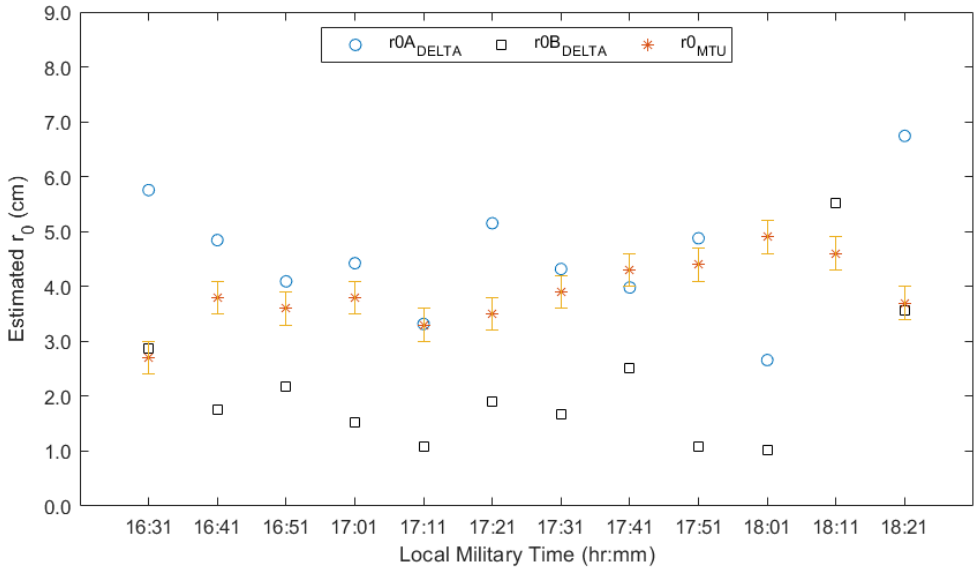

Figure A.3: Comparison of Estimated r_0 over Time for 03-02-2020